HHS Public Access

Author manuscript

Biochim Biophys Acta Gen Subj. Author manuscript; available in PMC 2022 May 01.

Published in final edited form as:

Biochim Biophys Acta Gen Subj. 2021 May ; 1865(5): 129845. doi:10.1016/j.bbagen.2021.129845.

Mitochondrial fission factor (*Mff*) is required for organization of the mitochondrial sheath in spermatids

Grigor Varuzhanyan[1], **Hsiuchen Chen**[1], **Rebecca Rojansky**[1], **Mark S Ladinsky**[1], **J. Michael McCaffery**[2], **David C. Chan**[1,*]

[1]Division of Biology and Biological Engineering, California Institute of Technology, Pasadena, CA 91125, USA.

[2]Integrated Imaging Center, Department of Biology, Johns Hopkins University, Baltimore, MD 21218.

Abstract

Background: Mitochondrial fission counterbalances fusion to maintain organelle morphology, but its role during development remains poorly characterized. Mammalian spermatogenesis is a complex developmental process involving several drastic changes to mitochondrial shape and organization. Mitochondria are generally small and spherical in spermatogonia, elongate during meiosis, and fragment in haploid round spermatids. Near the end of spermatid maturation, small mitochondrial spheres line the axoneme, elongate, and tightly wrap around the midpiece to form the mitochondrial sheath, which is critical for fueling flagellar movements. It remains unclear how these changes in mitochondrial morphology are regulated and how they affect sperm development.

Methods: We used genetic ablation of *Mff* (mitochondrial fission factor) in mice to investigate the role of mitochondrial fission during mammalian spermatogenesis.

Results: Our analysis indicates that *Mff* is required for mitochondrial fragmentation in haploid round spermatids and for organizing mitochondria in the midpiece in elongating spermatids. In *Mff* mutant mice, round spermatids have aberrantly elongated mitochondria that often show central constrictions, suggestive of failed fission events. In elongating spermatids and spermatozoa, mitochondrial sheaths are disjointed, containing swollen mitochondria with large gaps between organelles. These mitochondrial abnormalities in *Mff* mutant sperm are associated

*Correspondence: dchan@caltech.edu.

Credit author statement

Grigor Varuzhanyan: Conceptualization, Investigation, Writing – original draft

Hsiuchen Chen: Investigation, Writing – Review & Editing

Rebecca Rojansky: Investigation

Mark S Ladinsky: Investigation

J. Michael McCaffery: Investigation

David C. Chan: Conceptualization, Supervision, Writing – Review & Editing, Funding acquisition

Competing interests

The authors declare no competing interests.

with reduced respiratory chain Complex IV activity, aberrant sperm morphology and motility, and reduced fertility.

Conclusions: *Mff* is required for organization of the mitochondrial sheath in mouse sperm.

General Significance: Mitochondrial fission plays an important role in regulating mitochondrial organization during a complex developmental process.

Keywords

mitochondrial fission; spermatogenesis; mitochondrial sheath

Introduction

The balance between mitochondrial fusion and fission regulates mitochondrial morphology and cell metabolism [1,2]. For some cell type, this balance maintains mitochondrial size, shape, and number in accordance with cell physiology. In the long processes of neurons, for example, mitochondria are maintained at a small size compatible with efficient transport along the long distances from the cell body to the nerve terminal [3]. However, the role of mitochondrial dynamics in regulating mitochondrial organization and distribution during development is less well understood.

Mitochondrial fission is a multistep process involving several cellular factors. In the initial phase, the endoplasmic reticulum (ER) constricts the mitochondrion with help from actin filaments [4,5]. Next, receptors on the mitochondrial outer membrane recruit DRP1 (Dynamin-related protein 1), which oligomerizes into a ring-like structure on the mitochondrial surface to further constrict and sever the mitochondrion. In mammals, DRP1 can be recruited by four different receptors: MFF (Mitochondrial fission factor), MID49 (Mitochondrial dynamics protein of 49 kDa), MID51 (Mitochondrial dynamics protein of 51 kDa), and FIS1 (Mitochondrial fission 1 protein), with the latter having only a minor role [6–8]. DNM2 was reported to mediate the final step in fission following DRP1 constriction [9], but this notion has been challenged [10,11]. Additionally, recent reports showed that mitochondrial contacts with lysosomes [12] and Golgi-derived vesicles [13] facilitate mitochondrial fission.

The molecular mechanisms that orchestrate mitochondrial fission have been mostly deciphered using cultured cells and the role of fission during development has remained largely unexplored. To this end, we explored the role of mitochondrial fission during the development of the male germline (spermatogenesis) in mice. Spermatogenesis is a highly complex differentiation process associated with several mitochondrial transformations [14]. This lengthy process can be divided into three major developmental programs: 1) mitotic amplification of spermatogonia, 2) meiotic division of spermatocytes to form haploid spermatids, and 3) morphological transformation of round spermatids into mature sperm, a process termed spermiogenesis [15]. During these developmental transitions, mitochondria undergo dramatic changes in morphology, distribution, and number [16]. Mitochondria are generally small and fragmented in spermatogonia, elongate and cluster around the nuage during meiosis, and fragment again in post-meiotic spermatids. Near the end of spermatid

maturation, small spherical mitochondria line up longitudinally on the axoneme of the midpiece[17]. These mitochondria elongate and tightly wrap around the axoneme in a coordinated manner to organize into a compact mitochondrial sheath that fuels sperm motility [17]. The molecular factors that drive these coordinated mitochondrial rearrangements are unknown.

Because mammalian spermatogenesis involves drastic changes to mitochondrial morphology and organization, it is a promising model for studying the role of developmentally regulated alterations to mitochondrial dynamics. Indeed, studies of mitofusins-deficient mice indicate that mitochondrial fusion is important for maintaining OXPHOS activity in differentiating spermatogonia and meiotic spermatocytes [18,19]. However, the role of mitochondrial fission during spermatogenesis remained largely unknown. *Drp1* knockout mice are embryonic lethal [20], and to our knowledge, a male germline-specific deletion of *Drp1* has not yet been made. We previously reported that mice homozygous for a gene-trap allele of *Mff* (*Mff*^{gt}) have reduced fertility and sperm count [21]. Therefore, *Mff*^{gt} mice provide a model system to decipher the role of mitochondrial fission during male germline development. Our analysis suggests that mitochondrial fission is required during spermiogenesis for proper formation of the mitochondrial sheath.

Results and Discussion

Mff^{gt} sperm have disjointed mitochondrial sheaths.

To visualize male germ cells within the seminiferous epithelium, we performed Periodic–acid Schiff staining in wild type (WT) and *Mff*^{gt} testis sections (Figure 1). *Mff*^{gt} testes do not exhibit any obvious degeneration of seminiferous tubules, and all major germ cell types —spermatogonia (SG), spermatocytes (SC), spermatids (ST), and spermatozoa (SZ)—are present, indicating that loss of *Mff* does not impair generation of any one cell type. To examine the ultrastructure of *Mff*^{gt} sperm, we isolated sperm from caudal epididymides and subjected them to scanning electron microscopy (SEM). *Mff*^{gt} sperm often had morphological abnormalities in the midpiece (Figure 2A, white arrows) and kinking in or near the midpiece (Figure 2A, yellow arrow). Because the mitochondrial sheath is a major component of the midpiece, we utilized a mitochondrially targeted Dendra2 (Dn) fluorescent protein [22] to examine mitochondrial structure in sperm (Figures 2B and 2C). WT sperm have abundant mitochondria tightly packed in the sperm midpiece with little or no gaps between adjacent organelles. In contrast, *Mff*^{gt} sperm have disjointed mitochondrial sheaths with gaps between adjacent organelles. Total mito-Dendra2 fluorescence is greatly reduced in *Mff*^{gt} sperm (Figure 2C). In addition, imaging of sperm by differential interference microscopy (DIC) showed prominent defects in overall sperm morphology (Figures 2D and 2E). Over 60% of *Mff*^{gt} sperm contain kinks, which are found in the midpiece (>15%), the principal piece (>40%), or the neck (>5%).

Mitochondria in *Mff*^{gt} sperm are sparse and swollen.

To visualize the ultrastructure of sperm mitochondria, we performed electron tomography of epididymal sections to generate three-dimensional renderings of mitochondrial sheaths (Figures 3A and 3B, and Videos 1–4). When mitochondrial sheaths are visualized in

longitudinal sections of WT sperm, thin, rod-like mitochondria can be seen tightly and uniformly wrapping around the sperm axoneme (Figure 3A and Videos 1–2). In contrast, mutant sperm have disjointed mitochondrial sheaths with great variation in mitochondrial morphology. Mutant mitochondria appear highly swollen, have increased transverse diameters, and are too sparse to pack into a uniform sheath. In transverse sections of sperm midpieces, mutant mitochondria are also slightly elongated compared to control (Figure 3B and Videos 3–4). These data suggest that in the absence of fission, aberrantly enlarged mitochondria are poorly recruited to the sperm midpiece and/or fail to properly wrap around the axoneme, resulting in disjointed mitochondrial sheaths. TEM analysis of spermatozoa in testis sections showed similar defects (Figure S1), indicating that spermatozoa contain defective mitochondria prior to their release into the epididymides.

Mff^{gt} is required for developmentally regulated mitochondrial fragmentation in spermatids.

We next visualized mitochondrial morphology in early stage spermatids before they form mitochondrial sheaths (Figure 4). Whereas round and elongating spermatids of WT mice almost invariably contain fragmented mitochondria, the vast majority of mutant round and elongating spermatids contain tubular mitochondria (Figures 4A–4C). To visualize mitochondrial ultrastructure, we performed transmission electron microscopy (TEM) of testis sections in WT and *Mff*^{gt} mice (Figure 4D–4F). Consistent with observations made using light microscopy, we find that most round spermatid mitochondria are small and fragmented. In contrast, more than 20% of mutant mitochondria exhibit an elongated and highly constricted morphology, suggestive of a fission defect. Almost 80% of round spermatids (31 out of 39) contained one or more constricted mitochondria (Figure 4F).

Mff^{gt} sperm have reduced respiratory chain Complex IV activity, motility, and fertility.

To examine sperm mitochondrial function, we examined respiratory chain activity in isolated sperm by histochemical analysis of respiratory chain Complex IV (cytochrome c oxidase; COX) and succinate dehydrogenase (SDH) enzyme activity (Figures 5A and 5B). COX activity is visualized by oxidation of 3,3'-Diaminobenzidine (DAB) by cytochrome *c* into a brown product that can be visualized by light microscopy. SDH activity is visualized by oxidation of succinate by SDH followed by reduction of Nitro blue tetrazolium chloride (NBT), which forms a dark blue precipitate. In WT sperm midpieces, strong and uniform COX and SDH staining indicated normal OXPHOS activity (Figure 5A; top and middle panels). When COX and SDH stains are done simultaneously, only COX activity can be seen because the DAB reaction product saturates the cell (Figure 5A; bottom panel). Midpiece mitochondria in mutant sperm have a greater than 20% reduction in COX staining and an almost 20% increase in NBT staining (Figures 5A and 5B). When COX and SDH are monitored simultaneously in mutant sperm, blue coloring was evident due to decreased COX staining and increased SDH staining. These results indicate reduced Complex IV activity in *Mff*^{gt} sperm. In other cell types with low COX/high SDH activity, such as mtDNA-deficient skeletal muscle, increased SDH activity is correlated with increased mitochondrial mass. However, *Mff*^{gt} sperm have reduced mitochondria mass (Figures 2B and 2C). Thus, the cause of the increased NBT staining in *Mff*^{gt} sperm is unclear, but previous studies have correlated increased NBT staining in spermatozoa with increased reactive oxygen species

(ROS) [23,24]. Therefore, future studies should examine whether *Mff*^{gt} sperm have increased ROS production.

Because reduced respiratory chain activity has been associated with reduced sperm motility [25], we used mito-Dendra2 to track sperm motility by time-lapse microscopy (Videos 5–6). Mutant sperm were significantly less motile compared to WT controls. Because *Mff*^{gt} mice are runted and exhibit severe cardiomyopathy [21], it is important to distinguish whether their reduced fertility is due to an inherent defect in sperm function or secondary to other health problems. To this end, we performed *in vitro* fertilization using sperm from WT/Dn and *Mff*^{gt}/Dn males with oocytes from WT females and tracked fertilization success by progression to the 2-cell stage (Figures 5C and 5D). WT sperm successfully fertilized 64.1% (21.5 out of 33.5) of WT oocytes. In contrast, mutant sperm failed to fertilize any oocytes (0 out of 35.75).

Conclusions

Recent studies have uncovered the importance of mitochondrial dynamics for male fertility [14,18,19,21]. Mitochondria in stem and progenitor spermatogonia are sparse, small, and spherical. However, as germ cells enter meiosis, mitochondria increase their numbers, cluster, and undergo fusion, which promotes OXPHOS [18]. The increase in OXPHOS at this time is likely necessary to drive the ATP-dependent processes associated with Meiotic Prophase I [26]. Following meiosis, mitochondria return to a fragmented state, presumably to facilitate transport and reorganization onto the sperm midpiece during spermatid maturation. In mature spermatids, small mitochondrial spheres are arranged around the sperm axoneme, elongate, and tightly wrap around the axoneme to form the mitochondrial sheath [17], which enables sperm motility by fueling dynein motors [27].

The data presented here indicate that mitochondrial fission is acutely activated in post-meiotic round spermatids, which have more fragmented mitochondria compared to earlier meiotic spermatocytes. However, in *Mff*^{gt} round spermatids, mitochondria fail to fragment, forming long, tubular mitochondria with striking constrictions that may represent trapped fission intermediates. Based on the disordered structure of mitochondrial sheaths in *Mff*^{gt} sperm, we suggest that fission is important for generating small mitochondrial fragments that can more easily be organized around the sperm midpiece to form the mitochondrial sheath. In *Mff*^{gt} mutants, it is likely that the aberrant organization of the mitochondrial sheath, along with reduced respiratory chain Complex IV activity, contribute to their reduced fertility.

Materials and methods

Generation of mice

All mouse experiments were approved by the California Institute of Technology Institutional Animal Care and Use Committee. WT/Dn (*Mff*$^{+/+}$; *Rosa26*$^{PhAM(+/excised)}$) and *Mff*^{gt}/Dn mice (*Mff*^{gt}; *Rosa26*$^{PhAM(+/excised)}$) were generating by crossing *Mff*$^{+/+}$ and *Mff*^{gt} mice with *Rosa26*$^{PhAM(excised/excised)}$ mice. *Mff*^{gt} mice, described previously [21], were maintained on a 129P2/OlaHsd and C57Bl/6J background and are available at the Mutant Mouse Resource

& Research Center (RRID: MMRRC_066700-UCD). *Rosa26*$^{PhAM(excised/excised)}$ mice were described previously [22] and are available at the Jackson Laboratory (#018397).

Periodic–acid Schiff (PAS) staining

Testes were fixed in Bouin's fixative overnight at 4°C, dehydrated in a 30–90% ethanol series, cleared in Xylenes, and embedded in paraffin. Tissue blocks were sectioned at 7 μm, deparaffinized, and rehydrated before staining. Slides were incubated with 1% periodic acid (Electron Microscopy Sciences (EMS); 19324–10) for 30 min at RT, washed in running water for 5 min, then rinsed in deionized water. Slides were incubated with Schiff's reagent (EMS; 260582–05) for 30 min at RT and washed as described above before counterstaining with Gill 2 Hematoxylin for 30 s at RT. Slides were washed in running water for 1 min, dehydrated with ethanol, cleared with xylene, then mounted using Cytoseal XYL mounting media (Thermo Fisher Scientific; 22–050-262).

Scanning electron microscopy (SEM)

Epididymides were minced in PBS and incubated at 37˚C for 15 minutes for sperm to swim out. Sperm cells were pelleted with gentle centrifugation at 400 *g* for 10 min at RT and washed once in PBS. The samples were resuspended in sodium cacodylate and fixed with 3.0% formaldehyde and 1.5% glutaraldehyde in sodium cacodylate buffer (0.1M sodium cacodylate containing 5 mM Ca^{2+} and 2.5% Sucrose at pH 7.4). Samples were washed 3X in sodium cacodylate buffer before proceeding to SEM. Cellulose-nitrate filter circles were overlaid/activated with 2% glutaraldehyde for 30' and subsequently washed three times with ddH_2O. Sperm were overlaid onto the cellulose-nitrate activated filters for 20'. Filters were washed gently 1X in 100 mM cacodylate buffer and fixed in Palade's OsO4 for 1 hr at 4°C by immersion in the fixative. Filters were then washed in ddH_2O and dehydrated through a graded series of ethanol to 100%, followed by 3X washes of 100% ethanol. Filters were then critical point dried in a Tousimis 795 critical point dryer, or washed 2X with hexamethyldisilazane and allowed to dry slowly at room temperature under the hood. Filters were mounted onto aluminum specimen stubs using carbon transfer tabs, grounded to the stub with silver paste, and sputtered with Pt for one minute in an Anatech Hummer 6.2 sputter coater. Stubs were then observed in an FEI Quanta 200 ESEM at a 10KeV under high vacuum.

Light microscopy and image processing

Confocal fluorescence images, videos, and differential interference contrast (DIC) images were acquired using an inverted Zeiss LSM 710 confocal microscope with a 60X Plan-Apochromat objective. For live-cell motility videos, cells were maintained at 37°C and 5% CO_2. Bright-field images for histology were acquired using an upright Nikon Eclipse Ni-E fluorescence microscope equipped with a Ds-Ri2 camera and CFI Plan Apochromat Lambda objectives. Z stacks were acquired, and all-in-focus images were created using the NIS Elements Extended Depth of Focus plugin. All images were processed using ImageJ. All image modifications were performed on entire images (no masking was used) and were performed identically between genotypes.

Transmission electron microscopy (TEM) of testis sections

Testes were dissected, cut at the poles and fixed for one hour at RT with 3% formaldehyde and 1.5% glutaraldehyde in sodium cacodylate buffer (0.1M sodium cacodylate containing 5 mM Ca^{2+} and 2.5% Sucrose at pH 7.4). Samples were washed 3X in sodium cacodylate buffer. Samples were then postfixed in Palade's OsO4, stained in Kellenberger uranyl acetate, dehydrated through a graded series of EtOH, and flat embedded in EMBED 812 (EMS). 80-nm testis sections were prepared on an ultramicrotome (UCT; Leica), collected onto 400 mesh high-transmission nickel grids, and poststained with lead citrate and uranyl acetate. Images were collected with a transmission electron microscope (Tecnai 12; FEI) operating at 100 kV and equipped with an Olympus Soft Imaging System (OSIS) digital camera (Megaview III; Olympus).

3D Electron tomography of epididymal sperm

Caudal epididymides were dissected and immediately fixed with cold 3% glutaraldehyde, 1% paraformaldehyde, 5% sucrose in 0.1 M sodium cacodylate trihydrate. Pre-fixed pieces of tissue were rinsed with fresh cacodylate buffer and placed into brass planchettes (Type A; Ted Pella, Inc, Redding, CA) prefilled with 10% Ficoll in cacodylate buffer. Samples were covered with the flat side of a Type-B brass planchette and rapidly frozen with a HPM-010 high-pressure freezing machine (Leica Microsystems, Vienna Austria). The frozen samples were transferred under liquid nitrogen to cryotubes (Nunc) containing a frozen solution of 2.5% osmium tetroxide, 0.05% uranyl acetate in acetone. Tubes were loaded into an AFS-2 freeze-substitution machine (Leica Microsystems) and processed at −90°C for 72 hr, warmed over 12 hr to −20°C, held at that temperature for 8 hr, then warmed to 4°C for 2 hr. The fixative was removed, and the samples were rinsed 4x with cold acetone, and then were infiltrated with Epon-Araldite resin (Electron Microscopy Sciences, Port Washington PA) over 48 hr. Samples were flat-embedded between two Teflon-coated glass microscope slides, and the resin polymerized at 60°C for 24–48 hr.

Flat-embedded epididymis samples were observed with a stereo dissecting microscope, and appropriate regions were extracted with a microsurgical scalpel and glued to the tips of plastic sectioning stubs. Semi-thick (400 nm) serial sections were cut with a UC6 ultramicrotome (Leica Microsystems) using a diamond knife (Diatome, Ltd. Switzerland). Sections were placed on Formvar-coated copper-rhodium slot grids (Electron Microscopy Sciences) and stained with 3% uranyl acetate and lead citrate. Gold beads (10 nm) were placed on both surfaces of the grid to serve as fiducial markers for subsequent image alignment. Grids were placed in a dual-axis tomography holder (Model 2040, E.A. Fischione Instruments, Export PA) and imaged with a Tecnai TF30ST-FEG transmission electron microscope (300 KeV) equipped with a 2k × 2 k CCD camera (XP1000; Gatan, Inc Pleasanton CA). Tomographic tilt-series and large-area montaged overviews were acquired automatically using the SerialEM software package (Mastronarde, 2005). For tomography, samples were tilted + /− 64° and images collected at 1° intervals. The grid was then rotated 90° and a similar series taken about the orthogonal axis. Tomographic data was calculated, analyzed and modeled using the IMOD software package (Kremer et al., 1996; Mastronarde, 2008) on MacPro computers (Apple, Inc, Cupertino, CA).

COX/SDH Enzyme Histochemistry

COX/SDH labeling was performed as described previously [28], with minor modifications. Briefly, sperm cells were isolated from the caudal epididymis as described above, placed onto glass slides, and dried under a ventilated hood. Slides were stained with COX buffer for 25 min at RT in the dark, washed twice with dH_20 for 5 min, then stained with SDH buffer at 37°C for 45 min in the dark. Slides were washed two more times with dH_20 and destained using a 30%–90%–30% acetone gradient. After two additional washes in dH_20, slides were mounted using Fluorogel.

Sperm motility

Cauda epididymides of *Mff*^{gt} and WT male littermates were dissected into 0.5 mL modified Tris-buffered medium (mTBM) pre-warmed to 37°C and 5% CO_2. mTBM was composed of 113.1 mM NaCl, 3 mM KCl, 7.5 mM $CaCl_2$, 5 mM sodium pyruvate, 11 mM glucose, 1 mM caffeine, and 20 mM Tris., as described before [29]. Sperm were released by mincing the tissue with a 26-gauge needle and incubated at 37°C and 5% CO_2 for 15 minutes to allow for swim out. After incubation, the tissue was removed, and the fluid was mixed gently and collected into 1 mL Eppendorf tubes. Sperm were washed twice by gentle centrifugation at 833 *g* for 5 minutes, resuspended in 0.5 mL mTBM, then incubated at 37°C and 5% CO_2 for 30 minutes for capacitation. Sperm were plated at 5×10^5 sperm/mL in Nunc Lab-Tek II Chambered Coverglass slides (154852, Thermo), and videos were acquired as described above.

In vitro fertilization

For oocyte and sperm collection and fertilization all media was pre-warmed to 37˚C at 95% humidity, 5% CO_2, 5% O_2, and 90% N_2. Ovarian stimulation was performed as described previously [30]. Briefly, female C57BL/6J mice between 21 and 25 days of age were injected intraperitoneally with 25 I.U. of PMSG (G-4877 Sigma) on day −2, followed by 5 I.U. of HCG (C-1063, Sigma) 48 hours later on day 0. Sperm were collected from the cauda epididymides of WT/Dn or *Mff*^{gt}/Dn mice into 0.5 mL of Fertiup medium (KYD-002–05-EX, Cosmo Bio USA) at 37˚C, counted with a hemocytometer, and capacitated at a concentration of $2–4 \times 10^6$ cells/mL for 1.5–2 hr at 37˚C, 95% humidity, 5% CO_2, 5% O_2, 90% N_2.

Primed females were anesthetized with Ketamine-Xylazine and oviducts were dissected into 0.5 mL of Cook's IVF medium (K-RVFE-50, Cooks) to wash, then transferred to 0.15 mL of Cook's IVF medium overlaid with mineral oil (M-8410, Sigma) into which the cumulus mass was released. Capacitated sperm were diluted to a final concentration of $1–2 \times 10^5$ sperm/mL in 0.2 mL CARD medium (KYD-003-EX, Cosmo Bio USA) overlaid with mineral oil, into which the cumulus mass was then transferred. The sperm and ova were co-incubated for 4–6 hours at 37˚C, 95% humidity, 5% CO_2, 5% O_2, and 90% N_2, transferred through four 0.15 mL washes of Cook's IVF medium overlaid with mineral oil, then cultured in 0.5 mL Cook's IVF medium at 37˚C, 95% humidity, 5% CO_2, 5% O_2, 90% N_2 for 16–18 hr, at which point presumptive embryos were examined for progression to 2-cell stage.

Quantification

Quantification of total Dn fluorescence in sperm midpieces was performed on confocal images in which the sperm midpiece had been cropped and straightened using ImageJ. Integrated density (mean times area) values were plotted. Dn intensity plots in Figure 2B are "column average plots" generated from entire midpieces that were straightened using ImageJ. Quantification of sperm morphology was performed under the 100X objective of an upright Nikon Eclipse Ni-E fluorescence microscope. Quantification of mitochondrial morphology in round and elongating spermatids from WT/Dn and Mff^{gt}/Dn mice was by done by scoring seminiferous tubule transverse sections that were circular and had an obvious lumen. Seminiferous tubules in which the majority of round or elongating spermatids contained tubular mitochondria were scored as "tubular". All others were scored as "fragmented".

Replicates and statistical reporting

Pairwise comparisons were made using the Student's *t*-test. When multiple pairwise comparisons were made from the same dataset, *p*-values were adjusted using the Bonferroni correction. Number of mice and replicates are indicated in figure legends. All outliers were included in the analysis. All data are represented as mean ± SEM. **** indicates p≤0.0001; *** indicates p≤0.001; ** indicates p≤0.01; * indicates p≤0.05.

Supplementary Material

Refer to Web version on PubMed Central for supplementary material.

Acknowledgements

We thank all members of the Chan Lab for helpful discussions. We thank the Caltech Kavli Nanoscience Institute for maintenance of the TF-30 electron microscope.

Funding

This work was supported by the National Institutes of Health (R35 GM127147). Grigor Varuzhanyan was supported by a National Science Foundation Graduate Research Fellowship (DGE-1144469) and a National Institutes of Health Cell and Molecular Biology Training Grant (GM07616T32). Mark S. Ladinsky was supported by the National Institute of Allergy and Infectious Diseases (NIAID) (2 P50 AI150464) (awarded to Pamela J. Bjorkman, Caltech).

References

[1]. Mishra P, Chan DC, Metabolic regulation of mitochondrial dynamics, J. Cell Biol. 212 (2016) 379–387. doi:10.1083/jcb.201511036. [PubMed: 26858267]

[2]. Chan DC, Mitochondrial Dynamics and Its Involvement in Disease, Annual Review of Pathology: Mechanisms of Disease. 15 (2020) null. doi:10.1146/annurev-pathmechdis-012419-032711.

[3]. Schwarz TL, Mitochondrial trafficking in neurons, Cold Spring Harb Perspect Biol. 5 (2013). doi:10.1101/cshperspect.a011304.

[4]. Friedman JR, Lackner LL, West M, DiBenedetto JR, Nunnari J, Voeltz GK, ER Tubules Mark Sites of Mitochondrial Division, Science. 334 (2011) 358–362. doi:10.1126/science.1207385. [PubMed: 21885730]

[5]. Korobova F, Ramabhadran V, Higgs HN, An actin-dependent step in mitochondrial fission mediated by the ER-associated formin INF2, Science. 339 (2013) 464–467. [PubMed: 23349293]

[6]. Chan DC, Fusion and Fission: Interlinked Processes Critical for Mitochondrial Health, Annual Review of Genetics. 46 (2012) 265–287. doi:10.1146/annurev-genet-110410-132529.

[7]. Losón OC, Song Z, Chen H, Chan DC, Fis1, Mff, MiD49, and MiD51 mediate Drp1 recruitment in mitochondrial fission, Mol. Biol. Cell. 24 (2013) 659–667. doi:10.1091/mbc.E12-10-0721. [PubMed: 23283981]

[8]. Otera H, Wang C, Cleland MM, Setoguchi K, Yokota S, Youle RJ, Mihara K, Mff is an essential factor for mitochondrial recruitment of Drp1 during mitochondrial fission in mammalian cellsMff is essential for mitochondrial recruitment of Drp1, J Cell Biol. 191 (2010) 1141–1158. doi:10.1083/jcb.201007152. [PubMed: 21149567]

[9]. Lee JE, Westrate LM, Wu H, Page C, Voeltz GK, Multiple dynamin family members collaborate to drive mitochondrial division, Nature. 540 (2016) 139–143. doi:10.1038/nature20555. [PubMed: 27798601]

[10]. Fonseca TB, Sánchez-Guerrero Á, Milosevic I, Raimundo N, Mitochondrial fission requires DRP1 but not dynamins, Nature. 570 (2019) E34–E42. doi:10.1038/s41586-019-1296-y. [PubMed: 31217603]

[11]. Kamerkar SC, Kraus F, Sharpe AJ, Pucadyil TJ, Ryan MT, Dynamin-related protein 1 has membrane constricting and severing abilities sufficient for mitochondrial and peroxisomal fission, Nat Commun. 9 (2018) 1–15. doi:10.1038/s41467-018-07543-w. [PubMed: 29317637]

[12]. Wong YC, Ysselstein D, Krainc D, Mitochondria-lysosome contacts regulate mitochondrial fission via RAB7 GTP hydrolysis, Nature. 554 (2018) 382–386. doi:10.1038/nature25486. [PubMed: 29364868]

[13]. Nagashima S, Tábara L-C, Tilokani L, Paupe V, Anand H, Pogson JH, Zunino R, McBride HM, Prudent J, Golgi-derived PI(4)P-containing vesicles drive late steps of mitochondrial division, Science. 367 (2020) 1366–1371. doi:10.1126/science.aax6089. [PubMed: 32193326]

[14]. Varuzhanyan G, Chan DC, Mitochondrial dynamics during spermatogenesis, J Cell Sci. 133 (2020). doi:10.1242/jcs.235937.

[15]. Griswold MD, Spermatogenesis: The Commitment to Meiosis, Physiological Reviews. 96 (2016) 1–17. doi:10.1152/physrev.00013.2015. [PubMed: 26537427]

[16]. De Martino C, Floridi A, Marcante ML, Malorni W, Scorza Barcellona P, Bellocci M, Silvestrini B, Morphological, histochemical and biochemical studies on germ cell mitochondria of normal rats, Cell and Tissue Research. 196 (1979) 1–22. [PubMed: 421242]

[17]. Ho H-C, Wey S, Three dimensional rendering of the mitochondrial sheath morphogenesis during mouse spermiogenesis, Microscopy Research and Technique. 70 (2007) 719–723. [PubMed: 17457821]

[18]. Varuzhanyan G, Rojansky R, Sweredoski MJ, Graham RL, Hess S, Ladinsky MS, Chan DC, Mitochondrial fusion is required for spermatogonial differentiation and meiosis, ELife. 8 (2019) e51601. doi:10.7554/eLife.51601. [PubMed: 31596236]

[19]. Zhang J, Wang Q, Wang M, Jiang M, Wang Y, Sun Y, Wang J, Xie T, Tang C, Tang N, Song H, Cui D, Chao R, Ding S, Ni B, Chen X, Wang Y, GASZ and mitofusin-mediated mitochondrial functions are crucial for spermatogenesis, EMBO Reports. 17 (2016) 220–34. doi:10.15252/embr.201540846. [PubMed: 26711429]

[20]. Wakabayashi J, Zhang Z, Wakabayashi N, Tamura Y, Fukaya M, Kensler TW, Iijima M, Sesaki H, The dynamin-related GTPase Drp1 is required for embryonic and brain development in mice, J. Cell Biol. 186 (2009) 805–816. doi:10.1083/jcb.200903065. [PubMed: 19752021]

[21]. Chen H, Ren S, Clish C, Jain M, Mootha V, McCaffery JM, Chan DC, Titration of mitochondrial fusion rescues Mff-deficient cardiomyopathyCardiac physiology restored in Mff/Mfn1 mutants, J Cell Biol. 211 (2015) 795–805. doi:10.1083/jcb.201507035. [PubMed: 26598616]

[22]. Pham AH, McCaffery JM, Chan DC, Mouse lines with photo-activatable mitochondria to study mitochondrial dynamics, Genesis. 50 (2012) 833–843. doi:10.1002/dvg.22050. [PubMed: 22821887]

[23]. Baehner RL, Boxer LA, Davis J, The biochemical basis of nitroblue tetrazolium reduction in normal human and chronic granulomatous disease polymorphonuclear leukocytes, (1976).

[24]. Tunc O, Thompson J, Tremellen K, Development of the NBT assay as a marker of sperm oxidative stress, International Journal of Andrology. 33 (2010) 13–21. doi:10.1111/j.1365-2605.2008.00941.x. [PubMed: 19076253]

[25]. Ruiz-Pesini E, Diez C, Lapeña AC, Pérez-Martos A, Montoya J, Alvarez E, Arenas J, López-Pérez MJ, Correlation of sperm motility with mitochondrial enzymatic activities, Clin Chem. 44 (1998) 1616–1620. doi:10.1093/clinchem/44.8.1616. [PubMed: 9702947]

[26]. Ranjha L, Howard SM, Cejka P, Main steps in DNA double-strand break repair: an introduction to homologous recombination and related processes, Chromosoma. 127 (2018) 187–214. doi:10.1007/s00412-017-0658-1. [PubMed: 29327130]

[27]. Serohijos AWR, Chen Y, Ding F, Elston TC, Dokholyan NV, A structural model reveals energy transduction in dynein, PNAS. 103 (2006) 18540–18545. doi:10.1073/pnas.0602867103. [PubMed: 17121997]

[28]. Ross JM, Visualization of mitochondrial respiratory function using cytochrome c oxidase/succinate dehydrogenase (COX/SDH) double-labeling histochemistry, Journal of Visualized Experiments : JoVE. (2011) e3266. doi:10.3791/3266. [PubMed: 22143245]

[29]. Park K-W, Niwa K, Bovine Oocytes Can Be Penetrated in Modified Tris-buffered Medium, Asian Australas. J. Anim. Sci. 22 (2009) 500–506. doi:10.5713/ajas.2009.80431.

[30]. Lois C, Hong EJ, Pease S, Brown EJ, Baltimore D. Germline transmission and tissue-specific expression of transgenes delivered by lentiviral vectors. Science 295 (2002) 868–872. doi:10.1126/science.1067081 [PubMed: 11786607]

Highlights

- *Mff* is required for mitochondrial fragmentation in post-meiotic spermatids.
- *Mff*−/− mitochondria have central constrictions, suggestive of failed fission events.
- Spermatozoa in *Mff*-deficient mice have discontinuous mitochondrial sheaths.
- Mutant mitochondria have reduced respiratory chain Complex IV activity.
- Mutant spermatozoa have aberrant morphology and reduced motility and fertility.

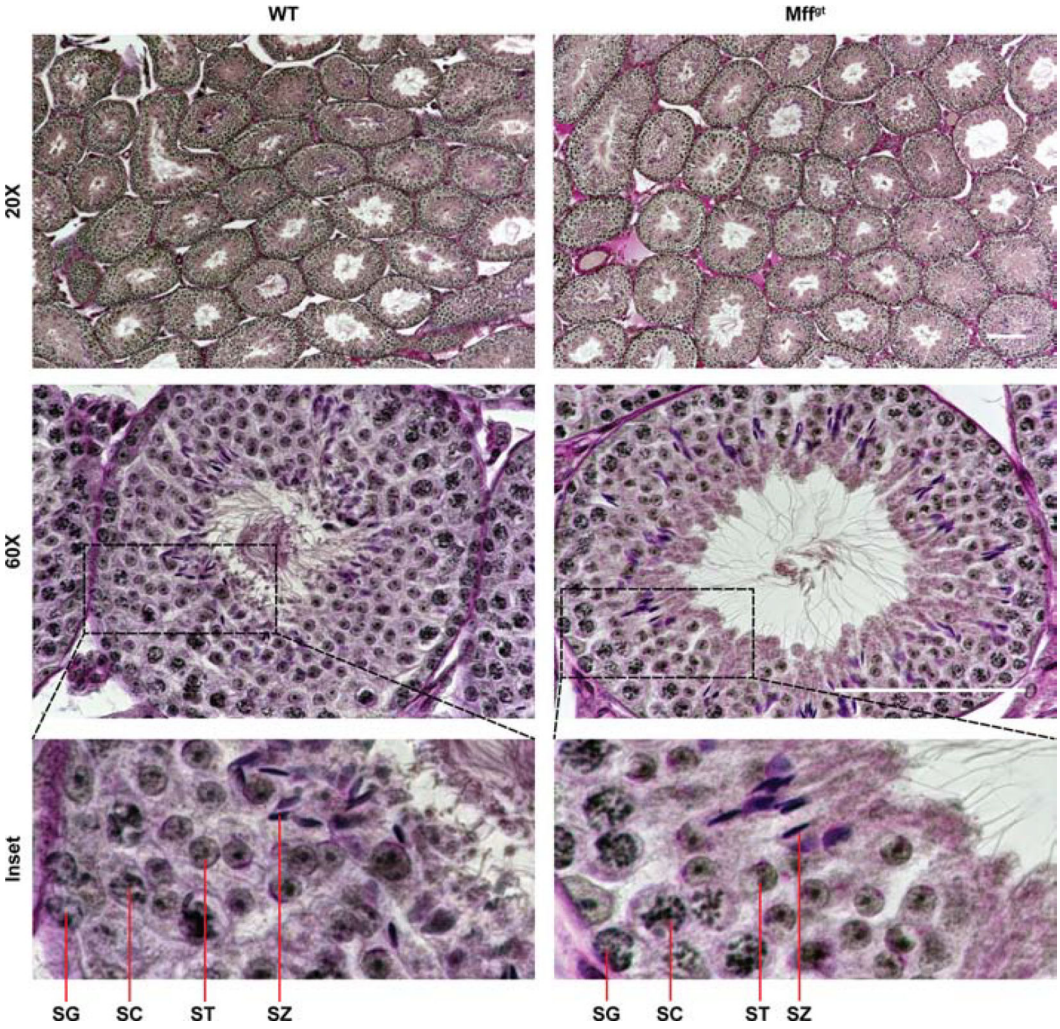

Figure 1. Histological analysis of seminiferous epithelium of *Mff*^{gt} mice.

Periodic-acid Schiff staining of Bouin's-fixed testis sections. Note that all major germ cell types are present in *Mff*^{gt} mice. SG, spermatogonium; SC, spermatocyte; ST, spermatid; SZ, spermatozoa. Scale bars, 50 μm.

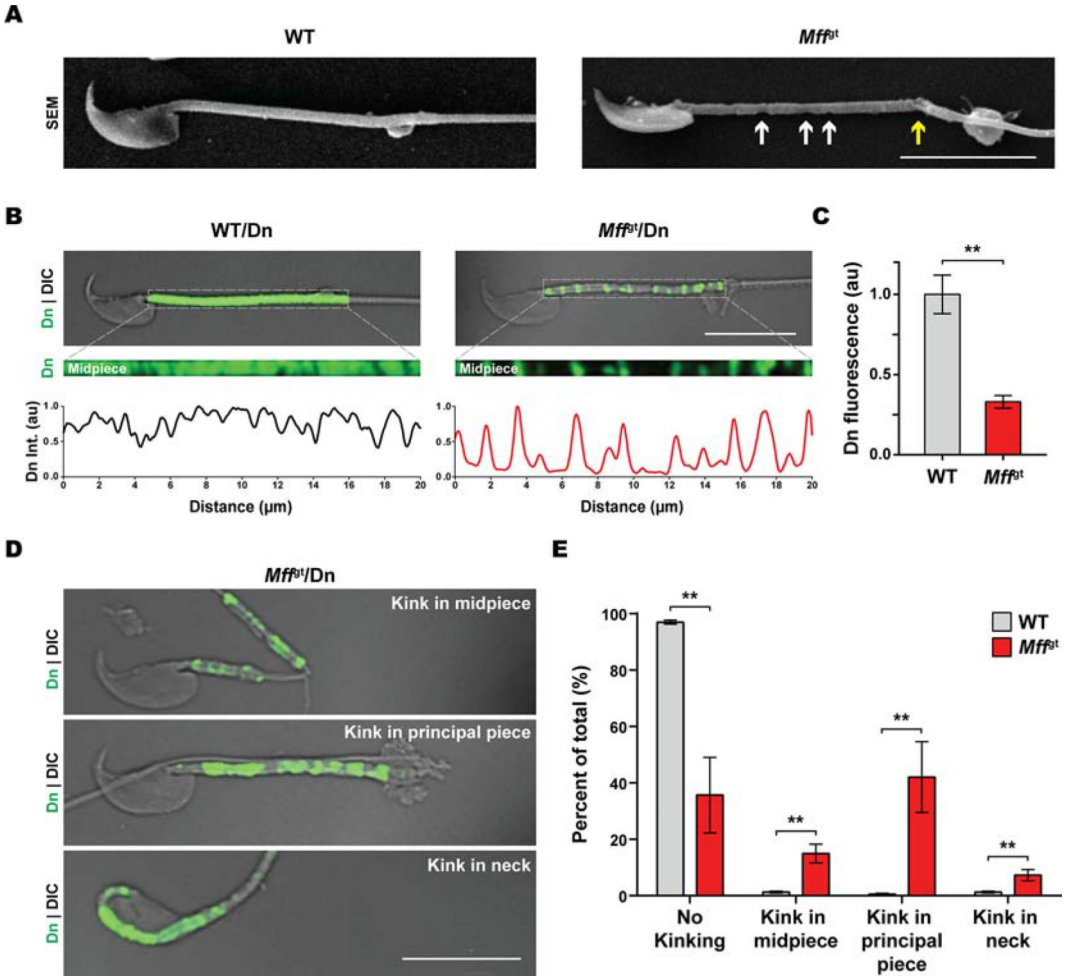

Figure 2. Visualization of mitochondrial sheaths in *Mff*^{gt}.

A) Scanning electron micrographs (SEM) of sperm isolated from the caudal epididymides. Note that the *Mff*^{gt} sperm cell has indentations in the midpiece and kinking at the distal end of the midpiece. Scale bar, 20 μm.

B) Top panel, DIC (direct interference contrast) and fluorescence micrographs of epididymal sperm. Green fluorescence comes from Dn (mito-Dendra2). Bottom panel, column average plot of Dn intensity along the length of the midpieces. Scale bars, 10 μm.

C) Quantification of total Dn fluorescence from sperm midpieces. At least 10 cells from each of four WT and four *Mff*^{gt} animals were quantified.

D) Representative examples of *Mff*^{gt} sperm exhibiting kinking in the midpiece, principal piece, and neck.

E) Quantification of sperm morphology. At least 100 cells from each of four WT and four *Mff*^{gt} were quantified. Data are represented as mean ± SEM. **p≤0.01. For statistical tests used, see the Materials and methods section.

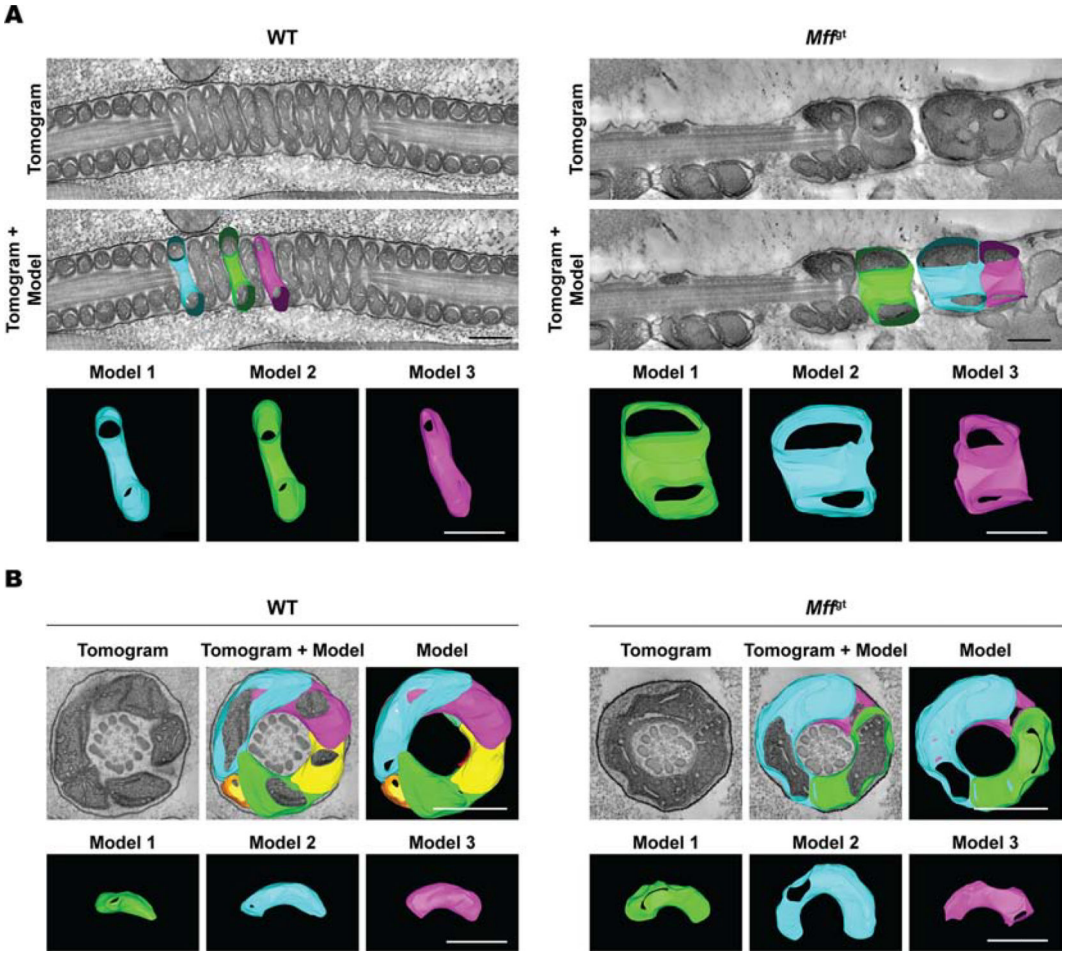

Figure 3. Ultrastructural analysis of *Mff*^{gt} mitochondrial sheaths

A) 3D electron tomography of longitudinal section of epididymal sperm. Note that *Mff*^{gt} sperm have wider mitochondria and large empty spaces where mitochondria should be present. For more information about the 3D renderings, see Videos 1–2.

B) 3D electron tomography of transverse section of epididymal sperm. For more information about the 3D renderings, see Videos 3–4.

Scale bars, 20 μm. For more information, see also Figure S1.

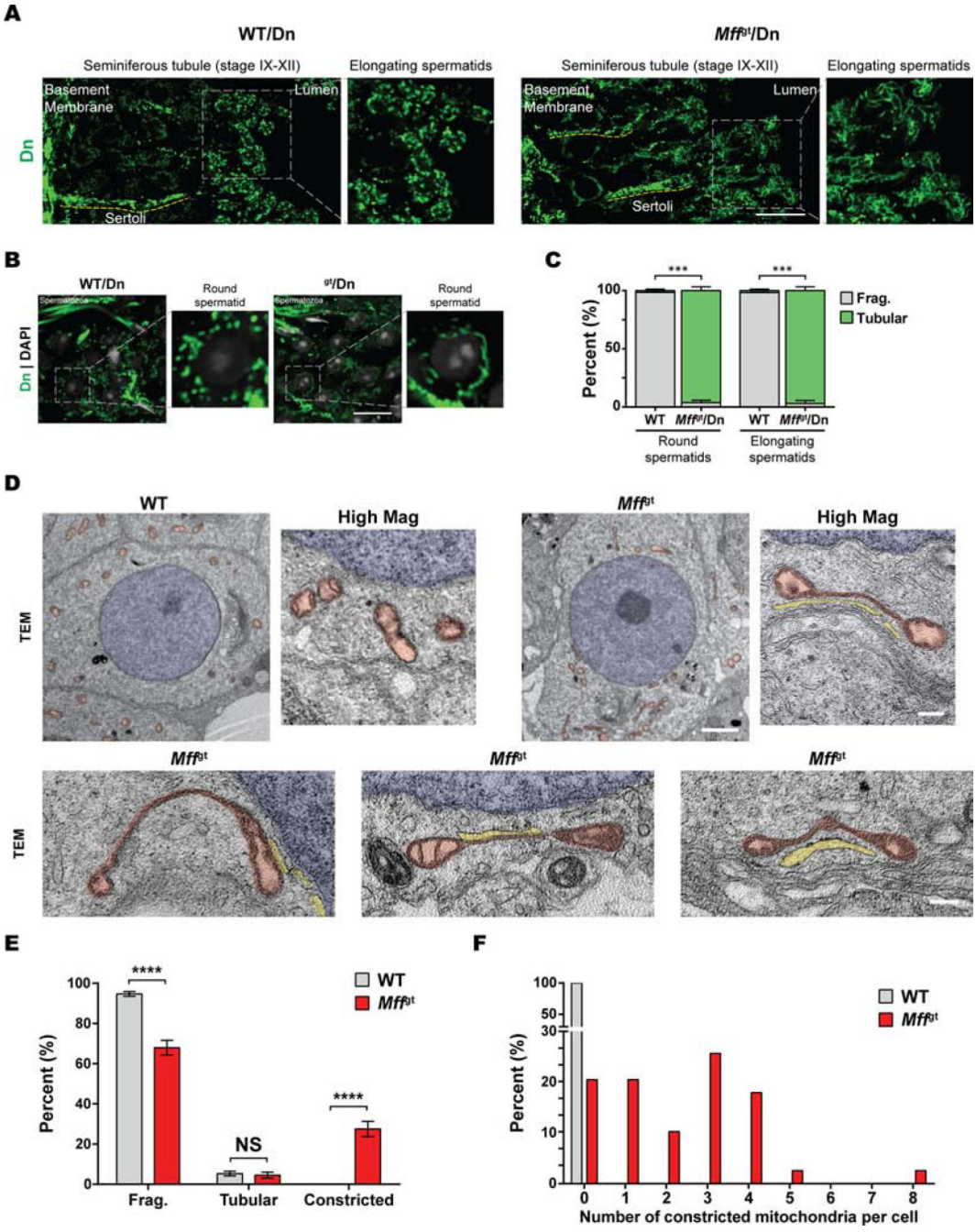

Figure 4. Mitochondrial morphology in *Mff*^{gt} round spermatids.

A) Mitochondrial morphology in round spermatids. Scale bar, 20 μm.

B) Mitochondrial morphology in elongating spermatids. Scale bar, 20 μm.

C) Quantification of mitochondrial morphology in round and elongating spermatids. At least 20 seminiferous tubule cross sections from each of two WT and three *Mff*^{gt} mice were scored.

D) TEM of round spermatids in testis sections. The following pseudocolors are used: nuclei, blue; mitochondria, red; ER, yellow. Low magnification panel scale bar, 5 μm. High magnification panel scale bars, 200 nm.

E) Quantification of mitochondrial morphology from TEM micrographs of round spermatids. A total of 36 cells from two WT mice and 39 cells from one *Mff*^{gt} mouse were quantified.

F) Frequency distribution of round spermatid mitochondria with aberrant constrictions. A total of 36 cells from two WT mice and 39 cells from one *Mff*^{gt} mouse were quantified. Data are represented as mean ± SEM. ***p≤0.001; **** p≤0.0001. For statistical tests used, see the Materials and methods section.

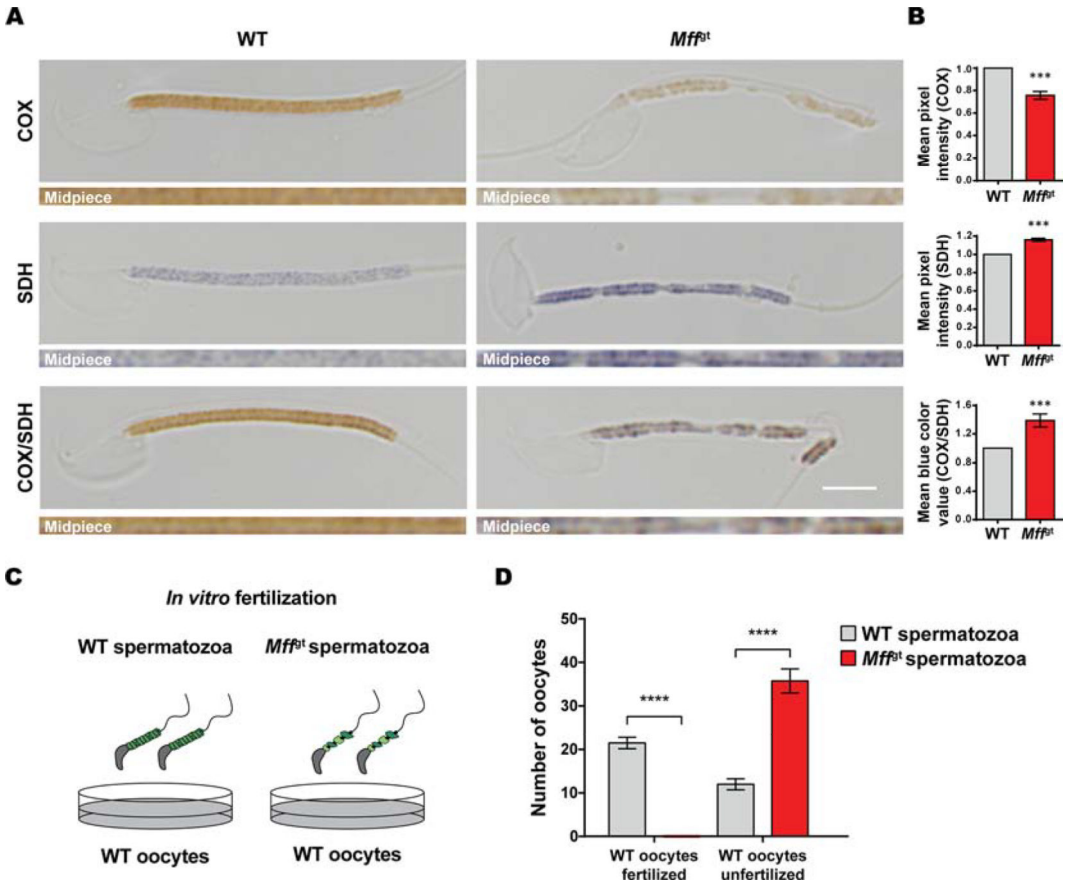

Figure 5. *Mff*^{gt} sperm have reduced Complex IV activity and reduced fertility.

A) COX and SDH staining of WT and *Mff*^{gt} sperm. Scale bar, 10 μm.

B) Quantification of COX and SDH staining. At least 10 cells from each of four WT and four *Mff*^{gt} mice were quantified.

C) Schematic of IVF experiment.

D) Quantification of IVF outcomes.

Data are represented as mean ± SEM. *** $p \leq 0.001$; **** $p \leq 0.0001$. For statistical tests used, see the Materials and methods section.